

# Numerical Simulations via Navier-Stokes Equation for Estimating Effects of Recess Geometry, Restrictor Dimension and Surface Speed on Static Characteristics of Hybrid Bearing

Te-Hui Tsai<sup>1</sup>, Cheng-Hsien Chen<sup>2</sup>, Yuan Kang<sup>3\*</sup>, and Yeon-Pun Chang<sup>3</sup>

<sup>1</sup> Department of Mechanical Engineering, Army Academy, Taoyuan 338, Taiwan.

<sup>2</sup> Department of Vehicle Engineering, Army Academy, Taoyuan 338, Taiwan.

<sup>3</sup> Department of Mechanical Engineering, Chung Yuan Christian University, Taoyuan 338, Taiwan.

## ABSTRACT

This paper researches the influences of two recess geometry and restrictor dimensions on the flow patterns and pressure distribution of lubricant film, which are coupled effects of hybrid characteristics of a hydrostatic bearing, by using the numerical simulation method. Analyze the results to understand the characteristics and the reasons of flow patterns of recess and calculate the loading capacity. The research gets the design parameter of increasing the loading capacity.

**Keywords:** hydrostatic bearing, capillary, recess, hybrid effect

## 由那維爾-史托克方程式模擬油腔幾何、節流器及表面速度對混壓軸承靜特性的影響

蔡德輝<sup>1</sup> 陳鎮憲<sup>2</sup> 康淵<sup>3\*</sup> 張永鵬<sup>3</sup>

<sup>1</sup> 陸軍專科學校機械工程系講師

<sup>2</sup> 陸軍專科學校車輛工程系副教授

<sup>3</sup> 中原大學機械工程學系教授

## 摘要

本研究使用數值模擬的方法，探討三油腔幾何形狀和節流器尺寸對靜壓軸承的混壓特性與表面速度在流場圖及壓力分布方面的耦合效應。分析流場圖的成因及特性和承載能力。由本研究的成果獲致良好的承載能力設計參數。

**關鍵字：**靜壓軸承，毛細管，油腔，混合效應

文稿收件日期 97.10.15; 文稿修正後接受日期 98.8.10.; \*通訊作者

Manuscript received October 10, 2008; revised August 10, 2009; \*Corresponding author

## I. INTRODUCTION

The hydrostatic bearings are requested to satisfy the operating conditions such as high speeds, high power supply and large lubrication film stiffness characteristics. The research of the flow structure in a closed, lid driven cavity has been treated extensively in the last few decades. As a part of the class of separated flows, the closed cavity problem has mainly a fundamental theoretical importance. In recent years there has been sustained activity towards improved modelling of the flow in a hydrostatic pocket. Most of the recent work has concentrated towards implicit lumped treatment of the pocket performance in the numerical environment of the total solution of the Reynolds equation for the entire hydrostatic bearing.

Numerous authors have analyzed the overall thermofluid and dynamic performance of the hydrostatic bearing. We shall mention here only a few. Sharma et al. [1] observed bearings which have four different recess shapes including a square recess bearing, a circular recess bearing, a triangular recess bearing and an elliptical recess bearing for their static and dynamic performance parameters which include minimum film thickness, flow rate, rotor dynamic coefficients and threshold speed. Braun et al. [2] performed 2-D numerical visualization experiments of the flow in a hydrostatic pocket concentrating on the effects of the pocket aspect ratio, position of the restrictor on the pocket floor, and the inclination of the restrictor with regard to the direction of rotation, the flow in the cavity was thoroughly mapped, and the appearance and development of central vertical cells (CVC) and pocket up stream and downstream secondary recirculation eddies was well documented. Braun and Dzodzo [3] also studied numerically the two-dimensional flow morphology under different pocket geometries and Reynolds number conditions. The authors have also systematically separated, and quantified the contribution of the Couette and Poiseuille effects to the pressure developed under the runner, as well as the variation of the pressure in the radial direction. Braun and Batur [4] visualized nonintrusively the flow in a hydrostatic pocket bearing by means of a full

flow field tracking method. They studied the nature of the flow patterns due to changes in the angular velocity of the shaft pocket inlet mass flow and bearing clearance. Sharma et al. [5] used the finite element method to compute the performance characteristics of a circular thrust pad hydrostatic bearing with circular, rectangular, elliptical and annular recesses. A comparative study of the various bearing configurations has been carried out vis-à-vis different compensating devices such as capillary, orifice, and constant flow valve restrictors so as to study the combined influence of the geometry shape of recesses and the compensating device on bearing performance. Braun et al. [6] studied 2-D and 3-D recess depth and feed-line problems of the laminar flow in hydrostatic journal bearing clearance. They have all conformed that the pressure distribution in the recess is not uniform, and inertia induced pressure drops occur at the pocket edges when the fluid flows outward. As the shaft angular velocity increases, the pressure in upstream portion decreases, then starts a process of a recovery in the central region, and exhibits a sharp increase in the downstream of recess. Braun and Dzodzo [7] used three-dimensional Navier-Stokes equations to describe a laminar flow in a shallow hydrostatic pocket with adjoined lands. Using the 3-D flow describes the effects of Couette dominated flow and Poiseuille dominated flow. Osman et al. [8] presented an experimental study to assess the performance characteristics of hydrostatic thrust bearings. They obtain the good agreement between predicted theoretical performance and that experimentally measured. Cheng and Rowe [9] have presented a selection strategy for the design of externally pressurized journal bearings. The strategy concerns the selection of bearing type and configuration, the fluid feeding device and the bearing material. Dzodzo et al. [10] studied the development of the flow and pressure maps in a shallow hydrostatic bearing pocket and, on a comparative basis, discuss the effects of the pocket-to-land exit geometry when it takes different shapes. Using the finite volume method gives the solution of Navier-Stokes equation. Singh et al. [11] studied the performance of an externally pressurized multirecess hydrostatic/hybrid flexible journal bearing system by varying the geometry shape

of recess and using the membrane flow valve restrictor as a compensating element. Using the finite element method solved the equation governing the flow of lubricant in a journal bearing and restrictor flow equation. They described the effect of recess shape, bearing flexibility and a method of compensation on the performance characteristics of a hydrostatic/hybrid journal bearing system. Garg et al. [12] presented a comprehensive review of develops in the design and application of hydrostatic and hybrid journal bearing systems during the last few decades. They critically discussed the parameters that significantly affect the static and dynamic performance of a journal bearing. Their work included coverage of recent publications in the literature pertaining to hydrostatic and hybrid journal bearings focusing on the influence of parameters. Chen et al. [13] had presented comparative studies of the influences of restriction effects of capillary and orifice, respectively, as well as land-width ratio on the stability of a rotor system supported by deep or shallow recessed hydrostatic/hybrid bearings. Helence et al. [14] dealt with the Navier-Stokes and bulk-flow analysis of hybrid bearings intended for using in aerospace applications. They investigated the pressure field in the recess of centered hybrid bearings with radial and angled injection by using a numerical Navier-Stokes analysis. The numerical predictions are compared with experimental data taken from the literature for radial and angled injection.

The works reviewed deal either with flow in a closed lid driven cavity, or the flow in an open cavity driven by a shear layer, or the flow in a cavity with a penetrating jet. In essence, what we propose to solve is a combination of the three basic cases reviewed in the introduction, and apply it to the geometry and scope of a hydrostatic pocket. The numerical simulations will evaluate the effects of the aspect ratio, the influence of the Reynolds number and the jet strength, as well as the couple effect of them on the flow patterns in the cavity and pressure on the lid.

## II. MATHEMATICAL MODEL

The assumption in the works is that the cavity width is much larger than its length or

depth, so that we can reduce the problem to a two-dimensional case. The process is steady state, and the fluid is Newtonian and incompressible. The nondimensional formulation of the equations of motion is obtained by normalizing all pockets' length with respect to clearance of bearing  $h$  and fluid velocity  $u$  and  $v$  with respect to runner velocity  $U$ . Then one can write the momentum equations as

$$\bar{u} \frac{\partial \bar{u}}{\partial x} + \bar{v} \frac{\partial \bar{u}}{\partial y} = -\Lambda \frac{\partial \bar{P}}{\partial x} + \frac{1}{R_m} \left( \frac{\partial^2 \bar{u}}{\partial x^2} + \frac{\partial^2 \bar{u}}{\partial y^2} \right) \quad (1)$$

$$\bar{u} \frac{\partial \bar{v}}{\partial x} + \bar{v} \frac{\partial \bar{v}}{\partial y} = -\Lambda \frac{\partial \bar{P}}{\partial y} + \frac{1}{R_m} \left( \frac{\partial^2 \bar{v}}{\partial x^2} + \frac{\partial^2 \bar{v}}{\partial y^2} \right) \quad (2)$$

where  $\bar{u} = u/U$ ,  $\bar{v} = v/U$ ,  $\bar{P} = P/P_s$ ,  $\Lambda = P_s/\rho U^2$ ,  $R_m = \rho U h/\mu$ ,  $(\bar{x}, \bar{y}) = (x, y)/h$ , while the continuity equation is the standard

$$\frac{\partial \bar{u}}{\partial x} + \frac{\partial \bar{v}}{\partial y} = 0 \quad (3)$$

The variational formulation of Eqs. (1) through (3) over an element in the domain  $\Omega$  is given by

$$Q_1 = -\frac{1}{R_m} \left( \frac{\partial \omega_1}{\partial x} \frac{\partial \bar{u}}{\partial x} + \frac{\partial \omega_1}{\partial y} \frac{\partial \bar{u}}{\partial y} \right) + \Lambda \frac{\partial \omega_1}{\partial x} P$$

$$\int_{\Omega} \left[ w_1 \left( \bar{u} \frac{\partial \bar{u}}{\partial x} + \bar{v} \frac{\partial \bar{u}}{\partial y} \right) + Q_1 \right] d\bar{x}d\bar{y} - \oint_{\Gamma} w_1 t_x ds = 0 \quad (4)$$

$$Q_2 = -\frac{1}{R_m} \left( \frac{\partial \omega_2}{\partial x} \frac{\partial \bar{v}}{\partial x} + \frac{\partial \omega_2}{\partial y} \frac{\partial \bar{v}}{\partial y} \right) + \Lambda \frac{\partial \omega_2}{\partial y} P$$

$$\int_{\Omega} \left[ w_2 \left( \bar{u} \frac{\partial \bar{v}}{\partial x} + \bar{v} \frac{\partial \bar{v}}{\partial y} \right) + Q_2 \right] d\bar{x}d\bar{y} - \oint_{\Gamma} w_2 t_y ds = 0 \quad (5)$$

$$\int_{\Omega} w_3 \left( \frac{\partial \bar{u}}{\partial x} + \frac{\partial \bar{v}}{\partial y} \right) d\bar{x}d\bar{y} = 0 \quad (6)$$

where  $w_1$  (variation in  $\bar{u}$ ),  $w_2$  (variation in  $\bar{v}$ ),  $w_3$  (variation in  $P$ ) are appropriate weight function and  $t_x$ ,  $t_y$  denote the general boundary condition in the boundary domain  $\Gamma$  in the  $x$  direction and  $y$  direction, respectively. Over a typical element in  $\Omega$ , we approximate  $u$ ,

v and P by interpolation of the form

$$\bar{u} = \sum_{i=1}^r \bar{u}_i \psi_i, \quad \bar{v} = \sum_{i=1}^r \bar{v}_i \psi_i, \quad \bar{P} = \sum_{i=1}^s \bar{P}_i \phi_i \quad (7)$$

where  $\psi_i$  and  $\phi_i$  are interpolation functions of degree r and s ( $r > s$ ), respectively.

Substituting Eqs. (7) into Eqs. (4) to Eqs. (6) and selecting the weight functions being identical to the interpolation functions  $w_1 = \psi_i$ ,  $w_2 = \psi_i$ ,  $w_3 = \phi_i$ , that is, Galerkin weighted residual finite element scheme and integrating over an element gives

$$\begin{bmatrix} [k^{11}] & [k^{12}] & [k^{13}] \\ \text{sym.} & [k^{22}] & [k^{23}] \\ & & [k^{33}] \end{bmatrix} \begin{Bmatrix} \bar{u} \\ \bar{v} \\ \bar{P} \end{Bmatrix} = \begin{Bmatrix} \{F^1\} \\ \{F^2\} \\ \{0\} \end{Bmatrix} \quad (8)$$

where

$$[k^{11}] = \int_{\Omega} \psi_i \left( \bar{u} \frac{\partial \psi_i}{\partial x} + \bar{v} \frac{\partial \psi_i}{\partial y} \right) d\bar{x}d\bar{y} + \frac{1}{R_m} \int_{\Omega} \frac{\partial \psi_i}{\partial x} \frac{\partial \psi_j}{\partial x} d\bar{x}d\bar{y} + \frac{1}{R_m} \int_{\Omega} \frac{\partial \psi_i}{\partial y} \frac{\partial \psi_j}{\partial y} d\bar{x}d\bar{y}$$

$$[k^{12}] = [0], \quad [k^{22}] = [k^{11}], \quad [k^{33}] = [0],$$

$$F_i^1 = \oint_{\Gamma} t_x \psi_i ds, \quad F_i^2 = \oint_{\Gamma} t_y \psi_i ds$$

$$k_{ij}^{13} = \Lambda \int_{\Omega} \frac{\partial \psi_i}{\partial x} \phi_j d\bar{x}d\bar{y}, \quad k_{ij}^{23} = \Lambda \int_{\Omega} \frac{\partial \psi_i}{\partial y} \phi_j d\bar{x}d\bar{y}$$

$$i, j = 1, 2, \dots, r; \quad J = 1, 2, \dots, s$$

Clearly, the element coefficient matrix, and hence the global coefficient matrix, depends on the velocity field, which is not known a priori. Therefore, an iterative solution procedure is required. At the beginning of the first iteration, the velocity field is set to zero and the global equations are solved for the nodal velocities and pressure. In the second iteration, the coefficient matrices are evaluated using the velocity field obtained in the first iteration, and the assembled equations are solved again for the nodal velocities. This procedure is repeated until the velocity field obtained at the end of two consecutive iterations differs by a small preassigned number. The convergence criterion can be expressed as

$$\frac{\left[ \sum_{i=1}^n \left( |U_i^r - U_i^{r+1}|^2 + |V_i^r - V_i^{r+1}|^2 \right) \right]^{\frac{1}{2}}}{\left[ \sum_{i=1}^n \left( |U_i^{r+1}|^2 + |V_i^{r+1}|^2 \right) \right]^{\frac{1}{2}}} \leq 10 \text{ percent} \quad (9)$$

where  $(U_i^r, V_i^r)$  denote the velocity at node i at the end of iteration r.

### III. NUMERICAL SIMULATIONS

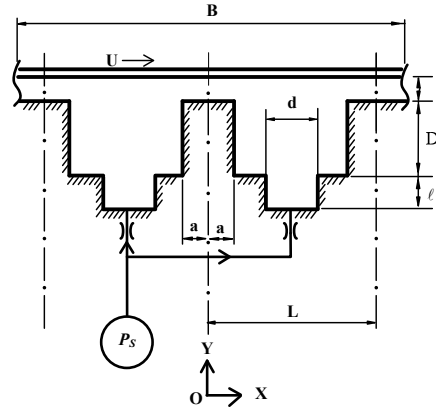


Fig.1. Geometry of the pocket.

Fig.1 shows a two-dimensional cross section of the analyzed hybrid journal bearing recess, including the supply area and the film lands. The fluid is considered as being incompressible and isothermal with  $\mu=0.09$  Pa·s and  $\rho=900$  kg/m<sup>3</sup>. The properties are those of oil and keeping density constant enables handling it as an incompressible fluid. The bearings had two identical and equally spaced deep pockets. The square pocket had a length of  $L=0.3$  m and a thickness of lubrication film  $h=200\mu\text{m}$ . A capillary restrictor fed each pocket. In all cases the runner was statically centered and the test matrix consisted of two runner speeds (21m/s, 1m/s) and three land/width ratio ( $\alpha$ ) and three diameter of capillary restrictor thus providing 12 working conditions. The working fluid was oil at constant temperature. An exhaustive description can be found in the above-mentioned publications. Basing on the analysis and discussions presented in this paper for the different bearings operating under identical conditions, the flow in the hydrostatic bearing was analyzed for all 12 working conditions by using a computational approach

based on the complete Navier-Stokes equation the domain are given in Table 1. To obtain a certain degree of generality the governing equations of motion and continuity, and the ensuing results are presented in a dimensionless form. In addition, a set of additional parametric geometric variables ( $\alpha \bar{B}$ ,  $\bar{h}$ ,  $\bar{L}$ ) were identified. The capillary restrictor is an important part of the hybrid bearing. If modeling this component for a complete Navier-Stokes analysis, optimal design is needed for obtaining the correct relation between the pressure drop and the flow rate. Moreover, the correct modeling of the capillary flow needs a refined grid and can lead to an important computational result.

The numeric analysis is based on the finite element method of the full Navier-Stokes equations. No slip boundary conditions are applied on the walls, which were considered as being smooth. A zero reference pressure is specified at the left and the right boundaries of the film lands. The supply pressure is 3MPa. The film lands were considered of sufficient length to ensure a completely developed thin flow. The recess working conditions is specified by the velocity of the moving wall. The modified Reynolds number characterizing the wall motion is one parameter used in the present work.

The present work started with the complete Navier-Stokes analysis of the bearing lubrication film flow. The present approach enabled to have higher analytical accuracy. This approach is liable to give more correct pocket pressure because it eliminates all the errors that could be introduced by modeling a capillary for which the design details only are approximately known.

The grid was of unstructured type and successive refinements were performed in order to obtain grid independent results. Cavitation was discarded the same as Sahlin etc. [15]. Cavitation was not taken into account because the goal of work was to enlighten the inertia effects, which determine the hydrostatic journal bearing (HJB) pressure pattern. The results should be relevant for HJB operating at surrounding pressures higher than the ambient one or working with a lightly compressible fluid.

To complete the formulation of the governing model and based on the geometry and conditions detailed in Fig.1, the associated boundary condition for the solution of Eqs. (1),

(2), (3) are developed below. The flow carried by the moving lid at the inlet and exit lands of the open cavity was considered as fully developed.

The appropriate boundary conditions divided pressure area and flow velocity into four parts, which are described individually by

- (1) The pressure on the boundaries was assigned to a reference environment pressure,  $\bar{P}=0$ , on the land's inlet and exit:

$$\bar{P}_{(\bar{x}=(\bar{B}/2+\bar{L}),\bar{y})} = \bar{P}_{(\bar{x}=(\bar{B}/2+\bar{L}),\bar{y})} = 0, \quad 0 \leq \bar{y} \leq 1.0$$

All the other pressures inside the domain were calculated taking the boundary pressure as the reference pressure.

- (2) The boundary conditions on the lands, at their open ends are:

$$\left( \frac{\partial \bar{u}}{\partial \bar{x}} \right)_{\bar{x}=(\bar{B}/2+\bar{L})} = \left( \frac{\partial \bar{u}}{\partial \bar{x}} \right)_{\bar{x}=(\bar{B}/2+\bar{L})} = 0, \quad 0 \leq \bar{y} \leq 1.0$$

The authors have been run preliminary tests to ensure that the lands were indeed long enough to generate a full-developed flow condition.

- (3) The boundary conditions at the driving lid are:

$$\bar{u}_{(\bar{x},\bar{y}=1.0)} = 1, \quad \bar{v}_{(\bar{x},\bar{y}=1.0)} = 0, \\ -(\bar{B}/2 + \bar{L}) \leq \bar{x} \leq (\bar{B}/2 + \bar{L})$$

During the parametric study, the non-dimensional velocity component in  $x$  direction of the runner is set to  $\bar{u} = 1$ . While, the velocity of the runner is set to  $U = 21$  m/s for the high-modified Reynolds number, and  $U = 1$  m/s for the low modified Reynolds number, respectively. The rest of the boundary conditions set the magnitudes of the velocity to  $\bar{u} = 0$  and  $\bar{v} = 0$  along the walls.

- (4) The pressure on the boundary is set equal to the supply pressure on each restrictor inlet:

$$\bar{P} = 1.0$$

The lubricant flows from the supply pump into a pressure control valve and then passes through the restrictor into the bearing recess. The pressure in the recess is therefore not equal to the supply pressure exiting the pump.

## IV. SIMULATION RESULTS AND DISCUSSION

### 4.1 Effects of the Reynolds number, and jet strength.

Fig.2 and Fig.3 present the effects of the Reynolds number on the flow pattern with three kinds of aspect ratio  $\alpha=0.05$ , 0.2 and 0.4 and restrictor diameter  $d_c=1\text{mm}$ . Fig. 2(a)-2(c) are the case in lower runner speed  $u=1\text{m/s}$  i.e.  $R_m=2$ , and Fig.3(a)-3(c) is the case in higher runner speed  $u=21\text{m/s}$  i.e.  $R_m=42$ . Two important phenomena are at work here. First, as runner speed is increased from  $1\text{m/s}$  to  $21\text{m/s}$ , the Couette effect becomes dominant and the flow that originally was outgoing (Fig.2(a)-2(c)) in the upstream section is completely turned around (Fig.3(a)-3(c)). Second, the main flow turn point in Fig. 2(a)-2(c) and 3(a)-3(c), becomes an impingement point that recedes down the wall as runner speed increases. This observation has significant potential importance in the design process of the cavity wall profile, especially in the regions adjacent to the lands.

Table 1. Bearing operating and geometry parameters

Type of restrictors	capillary
Restriction parameters ( $\delta_c$ )	$\delta_c = 0.737,$ 0.092 and 0.006
Recess depth ratio ( $\bar{h}_r$ )	20
Diameter of buffer pocket ( $d$ )	5 (mm)
Diameter of capillary ( $d_c$ )	1.0, 0.5 and 0.2 (mm)
Length of buffer pocket ( $\ell$ )	15 (mm)
Length of capillary ( $\ell_c$ )	$50 d_c$ (mm)
Modified Reynolds number ( $R_m$ )	2 and 42
Runner velocity ( $U$ )	1 and 21 (m/s)
Land-width ratio ( $\alpha$ )	0.05, 0.2 and 0.4
Jet-strength coefficient ( $\Lambda$ )	1111 and 52
For $\rho = 900\text{kg/m}^3$ , $\mu = 0.09\text{Pa}\cdot\text{s}$ , $P_s = 3\text{MPa}$ and $h = 0.2\text{mm}$	

### 4.2 Effects of the cavity aspect ratio ( $\alpha$ ).

Fig.2 and Fig.3 present the effect of cavity aspect ratio on the flow patterns. Fig. 2(a)-2(c) and 3(a)-3(c) show the aspect ratio effects in different  $R_m$  and  $\Lambda$  when  $\alpha=0.05$ , 0.2 and 0.4 respectively. Two major qualitative changes can be observed. The first is the diminishing capability of the jet to penetrate against the motion of the plate and associated shear layer as  $\alpha$  increases from 0.05, to 0.2 and 0.4, Fig.3(a), 3(b) and 3(c). The second is the formation of small recirculation zones in the vicinity of the jet entrance zones. As  $\alpha$  is increased from 0.05 to 0.2 and 0.4 one can see that central vertical cells (CVC) has already moved in a central position and has grown in size. The upstream secondary eddies (USE) and downstream secondary eddies (DSE) occupy fully the cavity corners in Fig.3(a) but haven't the occasion in Fig.3(c) because Fig.3(a) land is larger than Fig.3(c). The major portion of the jet occupies the central part of the cavity, while the CVC is small and confined under the driving shear layer. One can observe flow patterns that have already become familiar from previous Figs. discussion, and conclude that the decrease in cavity land length makes the jet more prominent, and more coupled from each other as the cavity starts to resemble a stilling tank.

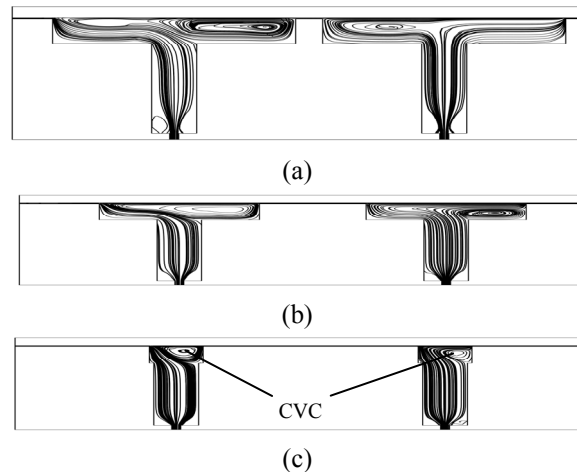


Fig.2. The typical flow patterns of low modified Reynolds number ( $R_m=2$ ) and relative large jet-strength coefficient ( $\Lambda=1111$ ) with capillary and orifice restrictors for (a)  $\alpha=0.05$  (b)  $\alpha=0.2$  (c)  $\alpha=0.4$

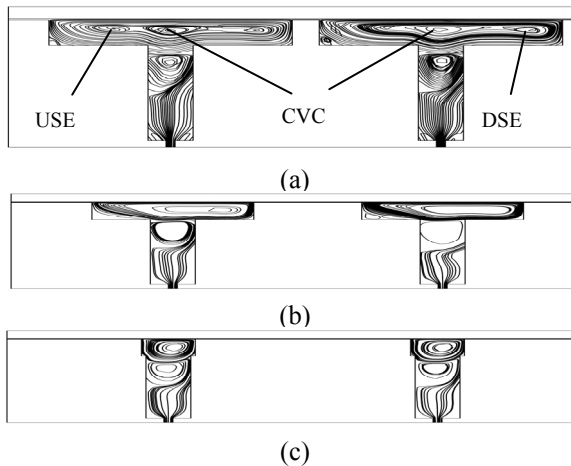


Fig.3. The typical flow patterns of high modified Reynolds number ( $R_m = 42$ ) with relative small jet-strength coefficient ( $\Lambda = 52$ ) for (a)  $\alpha = 0.05$  (b)  $\alpha = 0.2$  (c)  $\alpha = 0.4$

Fig.4 shows the flow patterns in the different restrictor diameter with  $R_m = 42$ ,  $\Lambda = 52$ ,  $\alpha = 0.05$ ,  $\bar{h}_r = 20$  for  $\delta_c = 0.737$ ,  $\delta_c = 0.092$  and  $\delta_c = 0.006$ . The vortical cell is increased with decrease in restrictor diameter. So we can deduce that bearing increase stability when restrictor diameter is increasing.

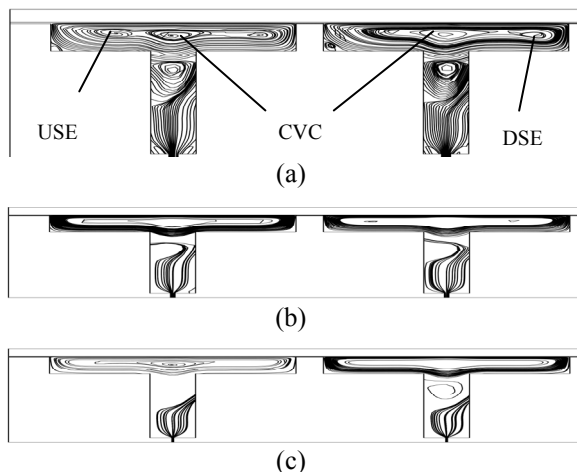


Fig.4. Flow patterns in the different restrictor diameter with  $R_m = 42$ ,  $\Lambda = 52$ ,  $\alpha = 0.05$ ,  $\bar{h}_r = 20$  for (a)  $\delta_c = 0.737$  (b)  $\delta_c = 0.092$  (c)  $\delta_c = 0.006$

Fig.5 shows the flow patterns in the different depth of pocket with  $R_m = 42$ ,  $\Lambda = 52$ ,  $\alpha = 0.05$ ,  $\delta_c = 0.737$  for  $\bar{h}_r = 20$ ,  $\bar{h}_r = 5$  and  $\bar{h}_r = 1$ . The hydrodynamic effect is obvious in

the shallow pocket i.e. Fig.5(c). Thus a higher pressure is needed to build up under the lid in order to move the fluid out of the pocket and onto the lands. One can conclude that in the shallow pocket, the CVC that filled the downstream region of the deep pocket is replaced by the modified vertical cell (MOVC), and by the flattened pillow recirculation region.

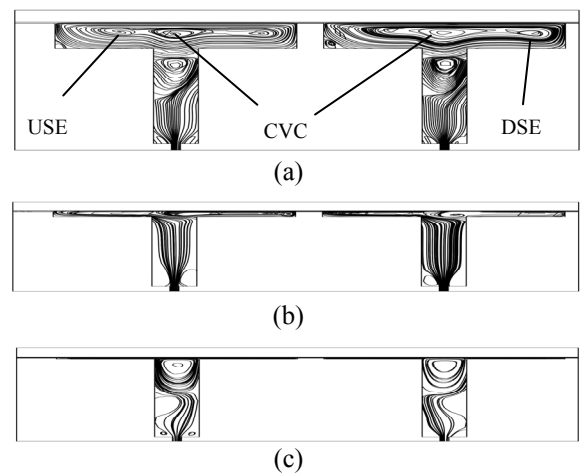


Fig.5. Flow patterns in the different depth of pocket with  $R_m = 42$ ,  $\Lambda = 52$ ,  $\alpha = 0.05$ ,  $\delta_c = 0.737$  for (a)  $\bar{h}_r = 20$  (b)  $\bar{h}_r = 5$  (c)  $\bar{h}_r = 1$

### 4.3 Pressure effects in the hydrostatic/hybrid cavity.

Fig.6 presents the variation of pressure, along the lid surface for the centered normal jet in a cavity with jet dominated flow  $R_m = 2$ ,  $\Lambda = 1111$ , and lid clearance  $h = 0.20\text{mm}$ . The effect of the jet dominates that of the moving plate and causes a symmetric distribution of pressures with respect to the center of the pocket, and the maximum pressure is generated in the region where the jet impacts the runner. This situation is supported by the flow pattern described in Figs 6(a), 6(b), and 6(c).

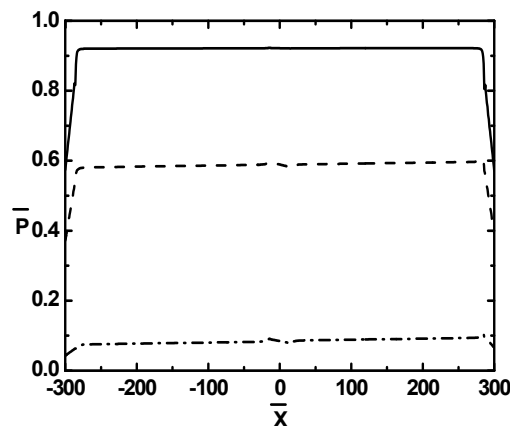
Fig.7 presents the Couette dominated flow on the development of the pressure profiles when the jet strength is kept constant with  $R_m = 42$ ,  $\Lambda = 52$ . In the right hand side of each of two pockets, a Rayleigh step effect is at work and the pressure rises locally with the increase in the Reynolds number. These results describe the hydrodynamic effect of oil film.

A comparison of the integrated areas below the pressure curves of Fig.8 and Fig.9, show that the load carrying capacity of a pocket grows with the decrease in the aspect ratio and with the increase in the diameter of restrictor. This figure represents a clear corollary of the study performed in Figs. 5.

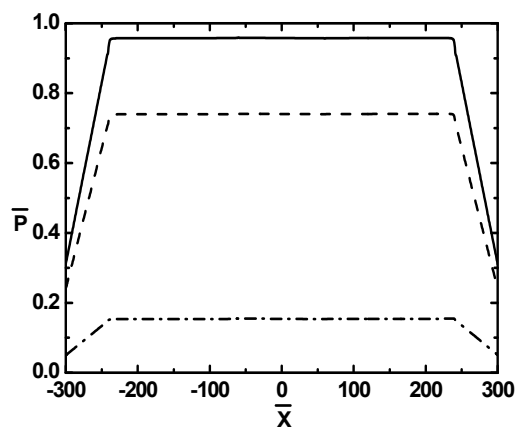
Fig.10 shows the circumferential pressure distribution along the runner with  $R_m = 2$ ,  $\Lambda = 1111$ ,  $\alpha = 0.2$ ,  $\delta_{c1} = 0.737$  for different film thickness. The decrease in  $h$  by decreasing 0.02mm in every time, (from 0.20 to 0.04), causes a most notable increase in the pressures magnitude. This is accompanied by a rather steep increase in the pressure.

Fig.11 shows the circumferential pressure distribution along the runner with  $R_m = 42$ ,  $\Lambda = 52$ ,  $\alpha = 0.2$ ,  $\delta_{c1} = 0.737$  for different film thickness. In deep pocket, one can conclude that when the flow is Couette dominated, the decrease in clearance has a major effect on the pressure spike at the downstream exit due to the Rayleigh step effect. The inertia pressure drop is clearly visible on the down slope of the spike, and it is attributed to the fluid acceleration as it enters the land. The reader can now easily deduce that the maximum of the spike occurs at the beginning of the downstream land. In shallow pocket, the back step effect is inexistent, while the Rayleigh step effect does not manifest through a localized spike, but rather contributes to a constant positive pressure slope. At the downstream exit of the pocket one can notice inertia pressure drops, which increase considerably with the decrease in clearance. Such large pressure drops can generate localized cavitation, depending on the associated thermodynamic conditions.

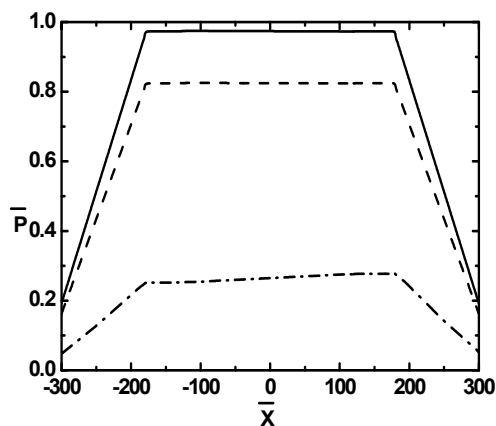
The jet impinging on the runner causes a maximum stagnation pressure, and the absence of a further rise in the downstream pressure is due only to the very weak Couette effect. One can conclude that the jet dominated flow generated much higher pressures than the Couette flow would, in both the deep and the shallow pockets. However, under Couette flow domination, the shallow pocket appears to generate pressures that are higher by approximately 10 percent, than the ones of the deep pocket.



(a)

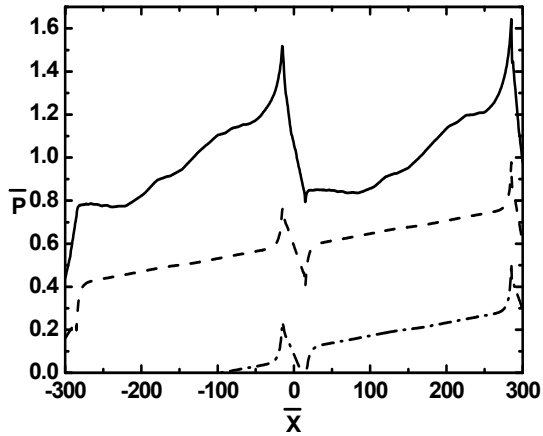


(b)

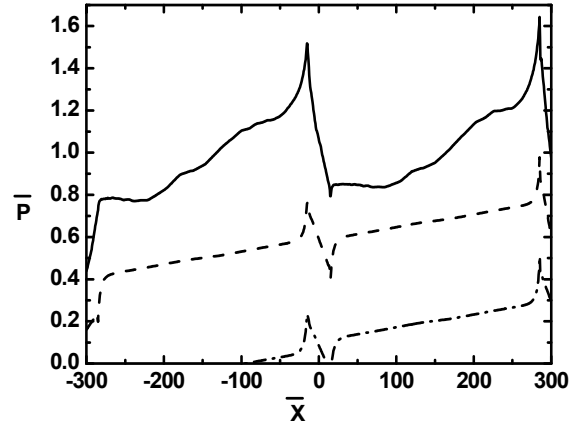


(c)

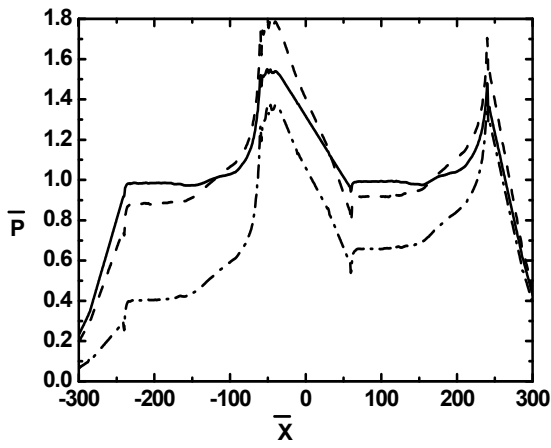
Fig.6. Pressure distribution under the runner for the jet dominated flow with  $R_m = 2$ ,  $\Lambda = 1111$  for (a)  $\alpha = 0.05$  (b)  $\alpha = 0.2$  (c)  $\alpha = 0.4$ ; ———  $\delta_{c1} = 0.737$ , - - - -  $\delta_{c2} = 0.092$ , - . . . -  $\delta_{c3} = 0.006$



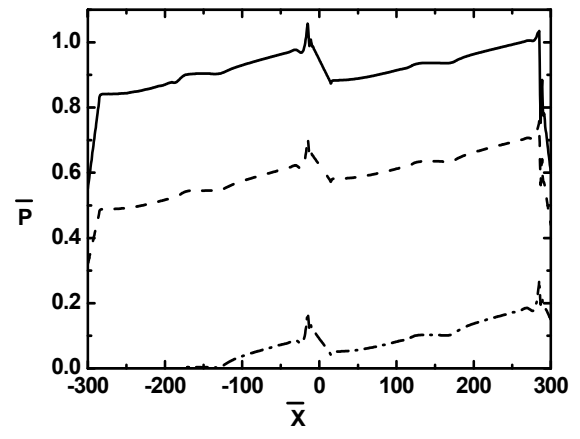
(a)



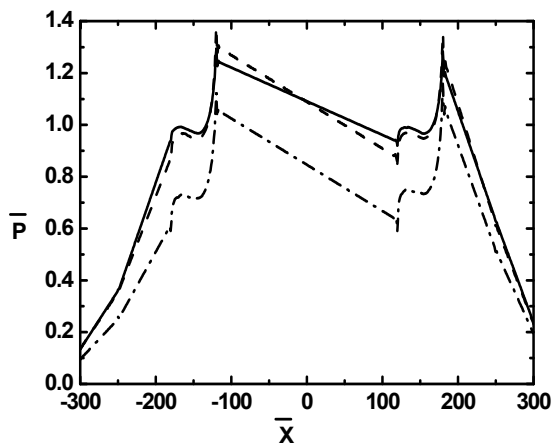
(a)



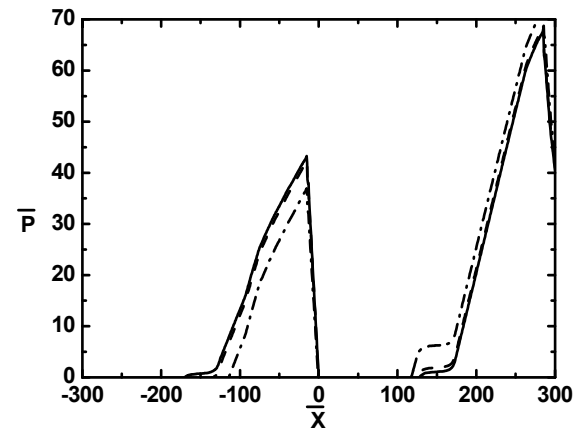
(b)



(b)



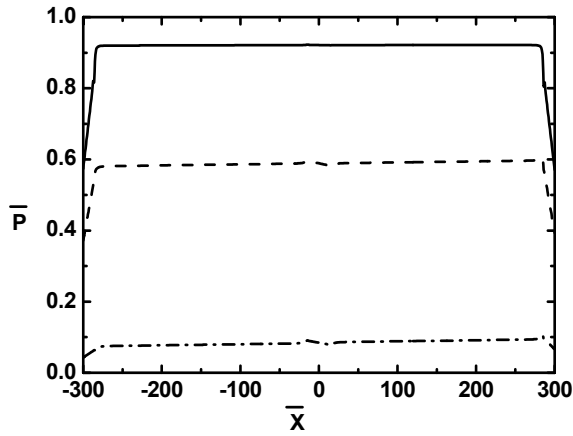
(c)



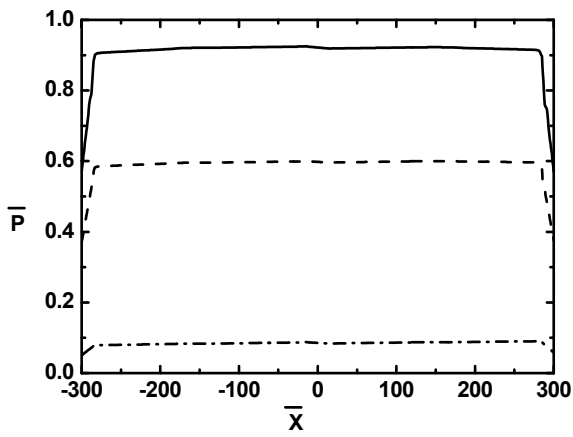
(c)

Fig.7. Pressure distribution under the runner for the Couette dominated flow with  $R_m = 42$ ,  $\Lambda = 52$  for (a)  $\alpha = 0.05$  (b)  $\alpha = 0.2$  (c)  $\alpha = 0.4$ ; —  $\delta_{c1} = 0.737$ , - - -  $\delta_{c2} = 0.092$ , - · - ·  $\delta_{c3} = 0.006$

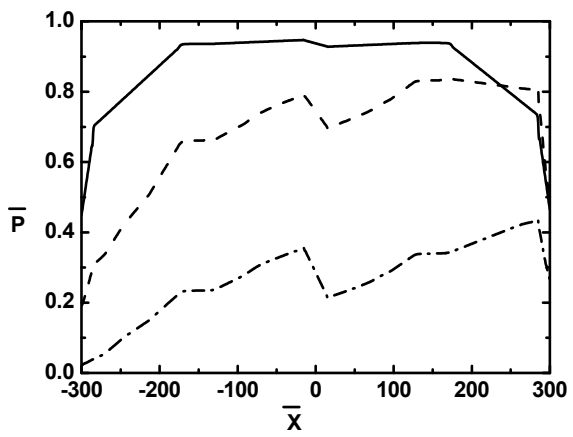
Fig.8. Pressure distribution under the runner for the Couette dominated flow with  $R_m = 42$ ,  $\Lambda = 52$  for (a)  $\bar{h}_r = 20$  (b)  $\bar{h}_r = 5$  (c)  $\bar{h}_r = 1$ ; —  $\delta_{c1} = 0.737$ , - - -  $\delta_{c2} = 0.092$ , - · - ·  $\delta_{c3} = 0.006$ ,  $\alpha = 0.05$ .



(a)

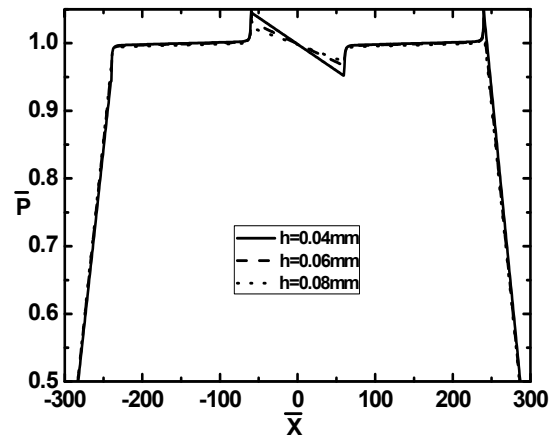


(b)

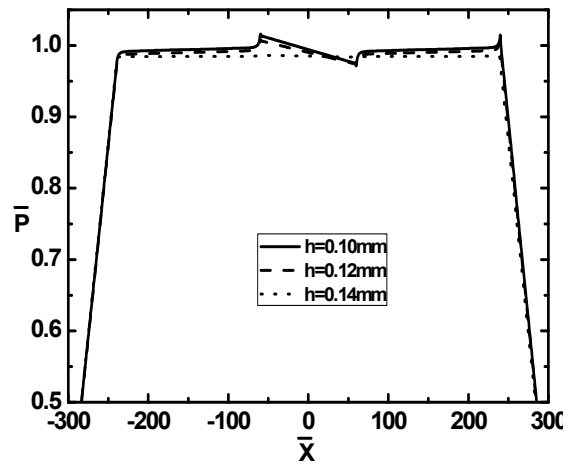


(c)

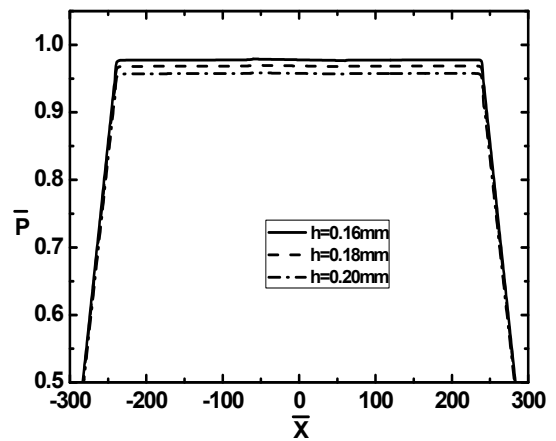
Fig.9. Pressure distribution under the runner for the jet dominated flow with  $R_m=2$ ,  $\Lambda=1111$  for (a)  $\bar{h}_r=20$  (b)  $\bar{h}_r=5$  (c)  $\bar{h}_r=1$ ; ———  $\delta_{c1}=0.737$ , - - -  $\delta_{c2}=0.092$ , - · - · -  $\delta_{c3}=0.006$ ,  $\alpha=0.05$



(a)

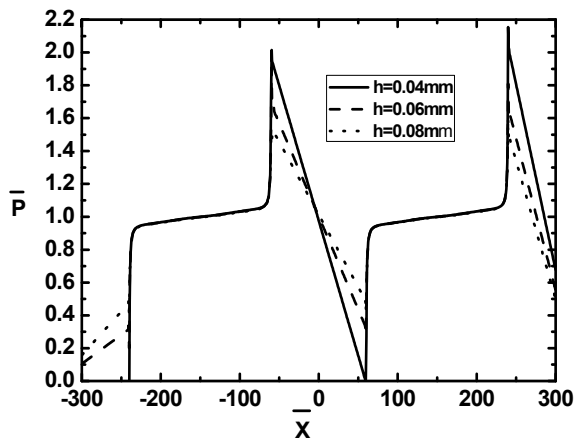


(b)

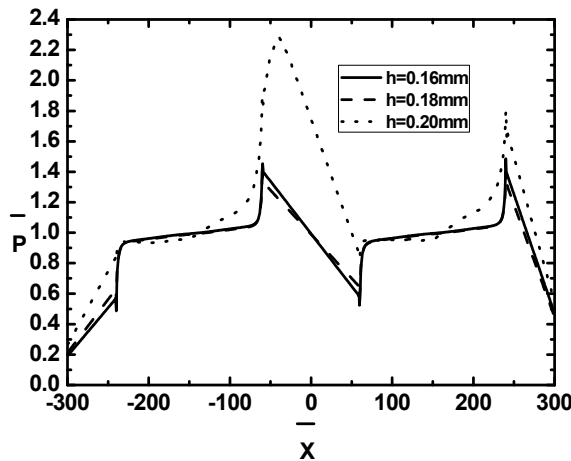


(c)

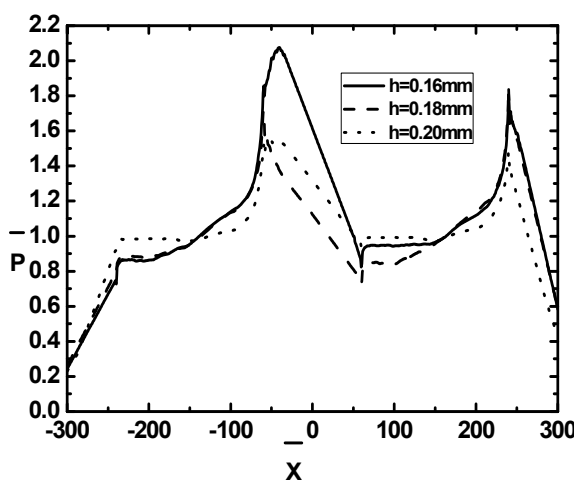
Fig.10. Pressure distribution under the runner with  $R_m=2$ ,  $\Lambda=1111$ ,  $\alpha=0.2$ ,  $\delta_{c1}=0.737$  for different film thickness



(a)



(b)



(c)

Fig.11. Pressure distribution under the runner with  $R_m = 42$ ,  $\Lambda = 52$ ,  $\alpha = 0.2$ ,  $\delta_{c1} = 0.737$  for different film thickness

## V. CONCLUSIONS

An analytical formulation using 2-D Navier Stokes equations is used for the determination of the flow patterns in an open lid driven cavity with a jet penetrating at the bottom of the cavity. The numerical solution uses the weighted residual Galerkin's method. A parametric study of the flow patterns and pressure in the hydrostatic pocket is presented. This study identifies both the geometric and dynamic parameters that control the hydrostatic behavior interplay.

The following general conclusions are drawn:

1. The performance of hydrostatic/hybrid bearing change appreciably as the geometric shape of the recess changes.
2. For the Poissuille dominated flow, the CVC with flattened recirculation pillow has become unsymmetrical and an excrescence of secondary vortex cell has filled the downstream region in each recess.
3. It can be found on all cases that a larger restriction parameter, which is corresponding to larger restrictor diameter, may provide larger hydrostatic effect as to increase the values of recess pressure. However, the recess pressure is increased with the increase of land-width ratio due to the hydrodynamic effect dominating over hydrostatic effect.
4. In low speed condition, the peak pressure is increased with decreasing the film thickness, and increased the pressure gradient. The value of peak pressure is decreased with increasing the film thickness, and decreased the pressure gradient. At last, the peak pressure is not decreased with increasing the film thickness when the pressure almost equal to supply pressure.
5. In high speeds condition, the magnitude of pressure has not positive relationship with film thickness.

## REFERENCES

- [1] Sharma, S. C., Jain, S. C. Singh, N. and Singh, S. K., "Performance of Hydrostatic/Hybrid Journal Bearings with Unconventional Recess Geometries," Tribol. Trans., Vol. 41, No. 3, pp. 375-381, 1998.

- [2] Braun, M. J., Choy, F. K., Zhou, Y. M., "The Effects of a Hydrostatic Pocket Aspect Ratio, Supply Orifice Position, and Attack Angle on Steady-state Flow Patterns, Pressure, and Shear Characteristics," *J. of Tribol., Trans. of the ASME*, Vol. 115, No. 4, pp. 678-685, 1993.
- [3] Braun, M. J. and Dzodzo, M. B., "Effects of the Feedline and the Hydrostatic Pocket Depth on the Flow Pattern and Pressure Distribution," *J. of Tribol., Trans. of the ASME*, Vol. 117, No. 2, pp. 224-233, 1995.
- [4] Braun, M. J. and Batur, C., "Non-intrusive Laser Based Full Field Quantitative Flow Measurement Aided by Digital Image Processing, Part 2: the Case of Hydrostatic Bearing," *Tribol. Int.*, Vol. 24, No. 5, pp. 277-290, 1991.
- [5] Sharma, S. C., Jain, S. C. and Bharuka, D. K., "Influence of Recess Shape on the Performance of a Capillary Compensated Circular Thrust Pad Hydrostatic Bearings," *Tribol. Int.*, Vol. 35, pp. 347-356, 2002.
- [6] Braun, M. J., Zhou, Y. M., and Choy, F. K., "Transient Flow Patterns and Pressure Characteristics in a Hydrostatic Pocket," *J. of Tribol., Trans. of the ASME*, Vol. 116, No. 1, pp. 139-146, 1994.
- [7] Braun, M. J., Dzodzo, M. B., "Three-dimensional Flow and Pressure Patterns in a Hydrostatic Journal Bearing Pocket," *J. of Tribol., Trans. of the ASME*, Vol. 119, No. 4, pp. 711-719, 1997.
- [8] Osman, T. A., Dorid, M., Safar, Z. S. and Mokhtar, M. O. A., "Experimental Assessment of Hydrostatic Thrust Bearing Performance," *Tribol. Int.*, Vol. 29, No. 3, pp. 233-239, 1996.
- [9] K. Cheng, W.B. Rowe, A selection strategy for the design of externally pressurized journal bearings, *Tribology International*, 28 (7) (1995) 465-474.
- [10] Dzodzo, M. B., Braun, M. J. and Hendricks, R. C., "Pressure and Flow Characteristics in a Shallow Hydrostatic Pocket with Rounded Pocket/land Joints," *Tribol. Int.*, Vol. 29, No. 1, pp. 69-76, 1996.
- [11] Singh, N., Sharma, S. C., Jain, S. C. and Reddy, S. C. "Performance of Membrane Compensated Multirecess Hydrostatic/hybrid Flexible Journal Bearing System Considering Various Recess Shapes," *Trib. Int.*, Vol. 37, pp. 11-24, 2004.
- [12] Garg, H. C., Sharma, H. B. and Kumar, V., "On the Design and Development of Hybrid Journal Bearings: a Review," *Tribotest*, Vol. 12, pp. 1-19, 2006.
- [13] Chen, C. H., Kang, Y., Chang, Y. P., Wang, Y. P. and Lee, H. H., "Influence of Restrictor on Stability of the Rigid Rotor-hybrid Bearing System," *J. of Sound and Vibration*, Vol. 297, No. 1, pp. 635-648, 2006.
- [14] Helene, M., Arghir, M. and Frene, J., "Combines Navier-Stokes and Bulk-flow Analysis of Hybrid Bearings Radial and Angled Injection," *J. of Tribol.*, Vol. 127, pp. 557-567, 2005.